Journal of Intelligent Manufacturing
https://doi.org/10.1007/s10845-024-02385-4

Image-based identification of optical quality and functional properties in inkjet-printed electronics using machine learning

Maxim Polomoshnov[1] · Klaus-Martin Reichert[1] · Luca Rettenberger[1] · Martin Ungerer[1] · Gerardo Hernandez-Sosa[2,3,4] · Ulrich Gengenbach[1] · Markus Reischl[1]

Received: 8 December 2023 / Accepted: 19 March 2024

Abstract

We propose a novel image-analysis based machine-learning approach to the fully-automated identification of the optical quality, of functional properties, and of manufacturing parameters in the field of 2D inkjet-printed test structures of conductive traces. To this end, a customizable modular concept to simultaneously identify or predict dissimilar properties of printed functional structures based on images is described and examined. An application domain of the concept in the printing production process is outlined. To examine performance, we develop a dataset of over 5000 test structures containing images and physical characteristics, which are manufactured using commercially available materials. Functional test structures are fabricated via a single-nozzle vector-based inkjet-printing system and thermally sintered. Physical characterization of electrical conductance, image capturing, and evaluation of the optical quality of the test structures is done by an automatic in-house built measurement station. Conceptionally, the design of a convolutional neural network is described to identify the optical quality and physical characteristics based only on acquired images. A mathematical apparatus that allows assessment of the identification accuracy is developed and described. The impact of printing resolution, of emerging defects in the geometry of printed structures, and of image quality and color space on the identification accuracy is analyzed. Quality groups related to the printing resolution that affect identification accuracy are determined. Supplementarily, we introduce not yet reported classification of processes related to the fabrication of printed functional structures, adopted from the process analytical technology.

Keywords Computer vision · Image analysis · Inkjet printing · Machine learning · Neural network · Printed electronics

Introduction

Functional inkjet printing

Over the recent decades, the inkjet-printing technology has not only been widely utilized in the labelling and graphical printing industry, but also found its usage in the state-of-the-art field of functional printing (Beedasy & Smith, 2020; Derby, 2010; Sirringhaus & Shimoda, 2003; Sowade et al., 2016; Yan et al., 2020). As a digitally-driven additive and non-contact fabrication technology, it enables deposition of a broad spectrum of functional materials directly on diverse substrates with minimum waste and contamination probability. In particular, the layer thickness in the nanometer to micrometer range is optimal for manufacturing of single electronic components, such as conductors, capacitors, resistors, diodes, and transistors; or of multilayer low voltage circuitries (Beedasy & Smith, 2020; Singh et al., 2013, pp. 207–235; Yan et al., 2020). Concurrently, a growing trend towards incorporating artificial intelligence (AI) into control, optimization, and maintenance of the drop-on-demand inkjet printing processes has been becoming visible during the last years (Brishty et al., 2022; Carou-Senra et al., 2023; Huang

✉ Maxim Polomoshnov
maxim.polomoshnov@kit.edu

1 Institute for Automation and Applied Informatics, Karlsruhe Institute of Technology (KIT), Eggenstein-Leopoldshafen, Germany

2 Light Technology Institute, Karlsruhe Institute of Technology (KIT), Karlsruhe, Germany

3 Institute of Microstructure, Karlsruhe Institute of Technology (KIT), Eggenstein-Leopoldshafen, Germany

4 InnovationLab, Heidelberg, Germany

Published online: 24 April 2024

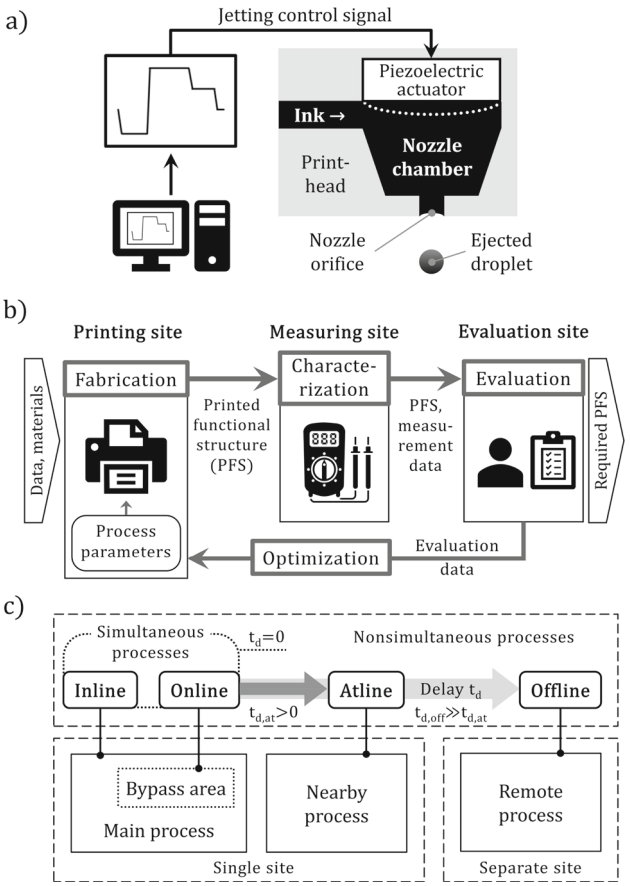

Fig. 1 **a** Schematic representation of the drop-on-demand inkjet-printing process and its main terms. **b** Conceptualized printed-electronics process flow, arrangement of its major stages and sites, and transferred outcomes, adapted from Hutchings et al. (2013, pp. 1–20), Kipphan (2001, pp.14–39), Teschner (2010, pp. 131–133). **c** Conceptualized process classification applied in this work, based on the mutual equipment disposition, and on the process simultaneity (unified and reinterpreted from Kim et al., 2021; Minnich et al., 2016; Patterson et al., 2023; Wenzel & Nirschl, 2015)

et al., 2020; Kim et al., 2022, 2023a, 2023b; Maîtrejean et al., 2022; Ogunsanya et al., 2021; Siemenn et al., 2022; Stoyanov & Bailey, 2017; Zhao et al., 2023).

A schematic representation of the drop-on-demand inkjet-printing process is depicted in Fig. 1a. One or multiple nozzles entailing a chamber and an electrically controlled actuator are an integral part of each inkjet printhead. By virtue of an electrical jetting control signal ("waveform"), displacement of a piezoelectric actuator occurs within the nozzle chamber, a fine ink droplet becomes ejected as a result. An adapted waveform is crucial for a smooth and stable ink droplet formation, and, further, for the entire printing process.

The printed-electronics process flow typically includes four stages—(a) fabrication (viz. preparation, printing, and subsequent functionalization during post-treatment), (b) characterization, (c) evaluation, and (d) optimization—carried out on three sites, as conceptualized in Fig. 1b. On the printing site, fabrication processes take place, impacted by various process parameters (e.g., ink and substrate properties, control signal, pre-treatment, equipment settings, ambient conditions, etc.). As a result, a printed functional structure (PFS) with the targeted functionality emerges. To attain the desired functional properties in the deposited ink, the post-treatment process is required (Hussain et al., 2023; Perelaer et al., 2010). On the measuring site, appearance and functional properties of the fabricated PFS are examined. On the evaluation site, the ultimate printout quality is assessed based on the measurement data, and on the PFS appearance. If necessary, process parameters are improved during the optimization stage, which is the back coupling between the evaluation and the printing sites—that implies re-manufacture of the PFS.

Process-relevant classification

In the process analytical technology, the following nomenclature of process-relevant methods is common: inline, online, atline, and offline. The main distinction of the methods is in the place of the physical connection between analyzers and the process (Kim et al., 2021; Minnich et al., 2016; Patterson et al., 2023; Wenzel & Nirschl, 2015). Considering printing as a compound process with the droplet ejection as its main constituent, the supplementary processes can be classified in the same manner, based on the mutual disposition of equipment and on the process simultaneity, as shown in Fig. 1c. Thus, (a) the inline process occurs directly in the printing area during the printing process (e.g., substrate heating), (b) the online in the vicinity during the printing process (e.g., measurement of ambient parameters); (c) the atline next to the printing area, with a minor delay in processing (e.g., waveform adjustment, droplet control, nozzle cleaning); (d) the offline in a separate space, with a noticeable delay in processing (e.g., virtually all pre- and post-treatment operations). The delay is usually caused by material, data, or the interim product transfer, or by other requisite technological steps.

Related work

Stoyanov and Bailey (2017) formulated a machine-learning (ML) based predictive approach targeted at additive manufacturing of conductive traces. The proposed algorithm was aimed at maintaining the optimal printed product quality, utilizing dynamically controlled manufacturing process data. Yan et al. (2019) applied ML algorithms to predict sheet resistance of inkjet-printed silver electrodes based on their digital images. Flaig and Zambal (2021) proposed deep-learning based algorithms for masking, defect detection, and optical quality evaluation of inkjet-printed lines. Siemenn et al.

(2022) integrated an AI-driven computer vision technique to develop a universal optimizing tool for droplet-generating devices, such as an inkjet printhead. Maîtrejean et al. (2022) employed neural networks for identification of the fluid-jet rheological properties with high accuracy. Huang et al. (2020) utilized a deep recurrent neural network to predict the ink droplet dynamics while inkjet printing, based on the drop-flow video data. Kim et al. (2022) developed and validated an AI-based algorithm to determine the optimal set of the waveform parameters for an unknown model ink. Kim et al., (2023a, 2023b) reported development of a jetting prediction model for viscoelastic inks using ML techniques. Ogunsanya et al. (2021) integrated a convolutional neural net (CNN) model and an image processing technique into an in-situ droplet monitoring to classify ejected ink droplets. Phung et al. (2023) integrated ML models to monitor jetting status of multi-nozzle printheads. Brishty et al. (2022) compared different ML models considering their prediction abilities in the field of printed electronics, with the focus on the droplet classification and the corresponding ink printability. Zhao et al. (2023) examined applicability of a bidirectional deep-learning model with a hybrid dataset (i.e., experimental and synthetic model data) for prediction of the additive manufacturing process parameters. Carou-Senra et al. (2023) studied a ML approach to predict printability and the ejected drug dose in the pharmaceutical inkjet printing. Kim et al., (2023a, 2023b) employed a residual neural net for an automatic visual monitoring of ejected ink droplets, using commercial functional ink. The proposed algorithm substantially enhanced classification speed and prediction accuracy compared to the uncompressed model. Kwon et al. (2023) developed a physics-added neural network algorithm, and improved identification of material physical characteristics in an inkjet-printing process. Shirsavar et al. (2022) evaluated electrical conductivity parameters of printed structures with respect to various printing process parameters. Hui et al. (2023) designed a neural net to predict quality and resistance of inkjet-printed silver lines in relation to various printing process parameters. Ivy et al. (2023) developed a ML-model to optically predict resistance of inkjet-printed resistors based on their geometry and texture features, using a high-resolution color scanner. Gafurov et al. (2022) utilized deep-learning algorithms for the optical quality assessment and parameter identification of screen-printed lines. Lall et al. (2023) developed a closed-loop control process for process parameter adjustments considering geometrical and electrical characteristics of printed traces, using particle-free inks. Tsai et al. (2023) reported an automatic ML-based optical inspection of functional properties of printed spiral antennas. Moon et al. (2023) employed ML and infrared images for quality inspection of aerosol-jet-printed functional structures.

Identified research gap

Although a lot of studies combining inkjet-printing with AI have been done, the large part of researchers remains focused on identification of separate PFS properties. Some researchers embedded AI into the droplet classification and into the automatic waveform optimization to mitigate disadvantages of the manual approach, such as incalculable time and labor cost, or an excess loss of expensive functional materials (Brishty et al., 2022; Huang et al., 2020; Kim et al., 2022, 2023a, 2023b; Ogunsanya et al., 2021; Phung et al., 2023; Zhao et al., 2023). In other surveys, one or several similar properties have been considered (Flaig & Zambal, 2021; Gafurov et al., 2022; Ivy et al., 2023; Moon et al., 2023; Tsai et al., 2023; Yan et al., 2019). Several research teams conducted a ML-based process parameter adjustment, based preliminarily on the printed-line geometry (Hui et al., 2023; Lall et al., 2023). Some property prediction schemes were proposed (Carou-Senra et al., 2023; Zhao et al., 2023), albeit not integrating any image information of the printed product.

Thus, the current state of research has not been yet systematically considering combination of the optical quality and of the functional properties of PFSs. Impact of printing resolution and of various factors outside of the system *printhead–nozzle orifice–ejected ink droplet* remains mostly out of sight of researchers. Among such factors, environmental parameters at the manufacturing and the measuring sites have to be pointed out. To our knowledge, no experimental study on the AI-based identification of multiple dissimilar process parameters from the image of inkjet-printed PFSs has been reported yet. Either, no extensive analysis of factors affecting such identification has been stated. Determination and analysis of such factors are essential for a successful integration of a high-speed, unbiased, damage-free, and automated AI-based quality control into printing processes. A simultaneous identification of multiple parameters with high accuracy contributes to reduction of fabrication waste, time, and costs. Conceptualization of the approach outlines a fundamental framework and designates avenues for further research. To bridge the identified gap, we proposed a universal concept, and aimed to prove its applicability and efficiency based on the use case of 2D inkjet-printed conductive traces.

Proposed concept

At present, the measuring and the evaluation sites are usually located atline or offline the printing site, the PFSs are evaluated mainly manually. This is time-consuming, onerous, prone to human error, and requires a high level of expertise (Carou-Senra et al., 2023). Sensitive printed samples

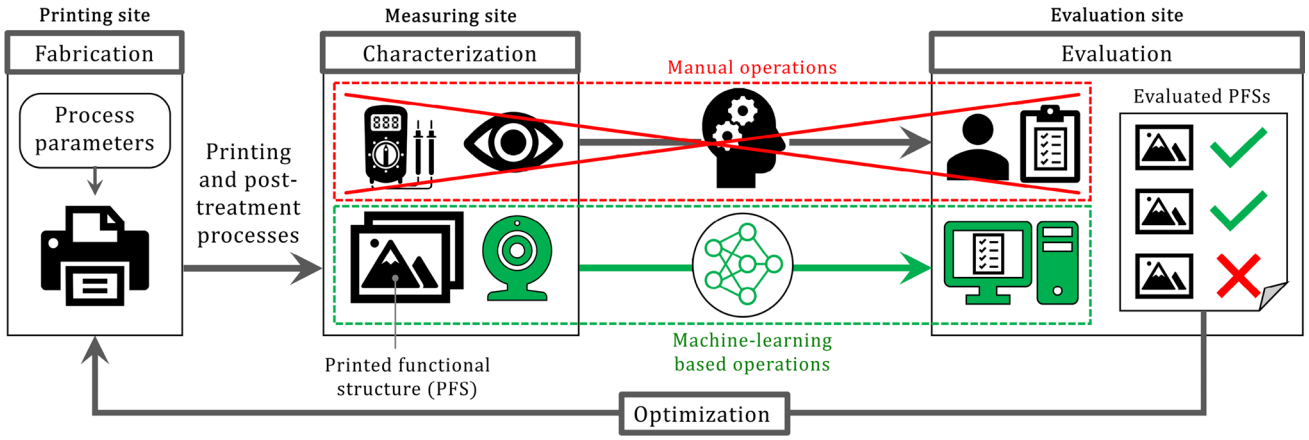

Fig. 2 Schematic representation of the proposed alterations in the contemporary approach to monitor PFS properties. After fabrication, PFS image has been collected, processed, and evaluated automatically using ML. Manual operations and human bias have been completely omitted

can be easily contaminated or damaged during transportation and processing, data related to single manufacturing steps can be lost by accident. In such events, retrieval of missed parameters (e.g., jetting frequency, post-treatment temperature, etc.) remains virtually impossible. We assumed that these issues could be resolved by means of an AI utilization instead of human labor. An added benefit would be the process shift and acceleration: inline or online the production site by AI-based operations instead of atline or offline by manual ones. The concept referred to the joint measuring and evaluation stages of the production chain with the following alterations: (a) automatic inline data collection (first and foremost, acquisition of PFS images under well-defined conditions), (b) contact-free measurements of PFSs to avoid their mechanical damage, (c) elimination of manual operations and human biases during evaluation of the acquired data, (d) systematic integration of ML-based operations. The proposed alterations are pointed out in Fig. 2.

At a broader level, the concept envisages a comprehensive embedding of ML-based techniques into functional printing, and, further, into smart manufacturing. Thus, various data domains serve interchangeably as input or output data in order to predict, identify, or rate the PFSs, applied materials, process parameters, etc., as illustrated in Fig. 3. For instance, based on the known manufacturing process parameters (i.e., data referring to the ink and substrate pre-treatment, the printing setup, and the product post-treatment), ink and substrate properties, and the printout shape, the printout quality control can be performed automatically (Fig. 3a). For specific process parameters, required functional properties, and desired PFS appearance, the ink and substrate properties can be defined or controlled (Fig. 3b). During set-up of the printing equipment, the PFS appearance can be forecast via available manufacturing process data and material properties, and required functional properties (Fig. 3c). Appropriate process parameters can be determined for printing of a PFS with a specific shape and functional properties, using ink and substrate combination with preset properties (Fig. 3d), which is particularly important for printed electronics (e.g., for electrode grids in photovoltaics, for printed antennas, and for interdigitated electrodes in printed field-effect transistors). Moreover, the concept has been expected to be applicable for a wide range of materials and techniques in the field of functional printing, far beyond sole inkjet printing of nanoparticle-based inks. In real applications where a plethora of influencing factors has to be reflected (Carou-Senra et al., 2023; Kwon et al., 2023; Shirsavar et al., 2022), the corresponding datasets can be easily tailored. In order to prove applicability and predictive power of the outlined concept, we focused on the idea highlighted in Fig. 3a.

Manuscript structure

This article encompasses six sections. The background information, findings of the literature survey, and description of the proposed concept are presented in the *Introduction* section. Research questions, objectives, and limitations of this work; methodology, applied data, and algorithm workflow; specification of printed structures; manufacturing, characterization, and data collection processes; and mathematical apparatus required for the assessment of the elaborated algorithm are outlined in the *Method* section. Results of the benchmarking of fabricated PFSs, results of the ML-based identification, and their brief evaluation are indicated in the *Results* section. Research outcomes, key factors, ways to increase identification accuracy and algorithm robustness, and further areas of application are scrutinized in the *Discussion* section. The key outcomes, and future work are summarized in the *Conclusion* section. Detailed technical and supporting data, not directly related to the considered proof of concept, are outlined in the *Supplementary Information* section (SI).

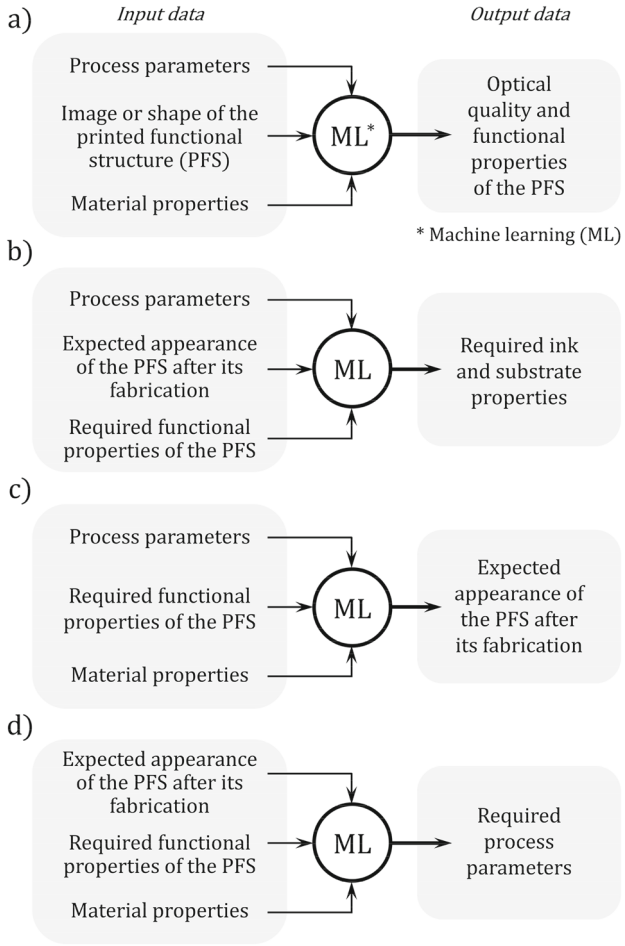

Fig. 3 Visualization of implied data links for potential application as a part of the proposed concept. Four major data domains ("modules") were defined, each three of which form the input data pool whereas the remaining fourth represents the target output data. With a pre-trained ML model, the target output data has to be subsequently evaluated or predicted, depending on the objectives. The module combination depicted in **a** was opted for be examined in this research

Method

Research questions, objectives, and limitations

To tackle the aforementioned problem of a high level of human-biased, contact-based manual operations in the printed-electronics fabrication, we formulated the following research questions. Addressing these questions facilitates bridging the research gap, and assisted our understanding of pros and cons of the evaluated concept.

Q1. Whether a simultaneous visual identification of dissimilar properties of inkjet-printed structures is applicable?
Q2. In what manner the contemporary approach to monitor properties of inkjet-printed structures must be modified for implementation of ML-based operations?
Q3. Whether a simple CNN-based algorithm is able to reliably identify the desired properties of inkjet-printed structures?
Q4. Whether and how printing resolution affects the identification accuracy?
Q5. Except for printing resolution, what further factors impact the identification accuracy?

To answer question Q1, we designed a plain CNN-based algorithm to identify four dissimilar properties of 2D inkjet-printed PFSs based on the image analysis. To answer question Q2, we examined the printed-electronics process flow to date, conducted a literature survey, and proposed an alteration concept. To answer question Q3, we customized and assessed the elaborated algorithm. Concordance between the actual and the AI-identified values of the PFS properties ("output accuracy") was opted as the main evaluation metrics. Additionally, for classification of Boolean variables, confusion matrix, accuracy, and F-score were utilized. An appropriate application of those metrics required preparation of a balanced dataset, which was achieved by preparation of a great number of PFSs. To answer question Q4, we examined PFSs with 60 different printing resolutions. To answer question Q5, we collected and discussed various factors, such as image quality, process parameters, and CNN parameters.

The key objectives set in this work were as follows:

- conceptualization of the contact-free ML-based approach to monitor product properties in the field of printed electronics,
- proof of the proposed concept in relation to 2D inkjet-printed conductive structures, based on a CNN-based algorithm,
- identification of crucial affecting factors that have to be thoroughly elaborated in future research.

This research had the following technological and methodological boundaries:

- printed-electronics domain represented by the flatbed 2D inkjet printing of a silver nanoparticle-based ink,
- single-nozzle, single-layer, vector-based printing in longitudinal direction,
- no consideration of complex PFS fabrication and evaluation methods as excessive and requiring standalone research (e.g., impact of printing at an angle, of multilayer printing, of utilization of numerous materials, of utilization of high-energy post-treatment methods, and of cross-section or profile measurement),
- comparison and selection of the best-performance ML-method required standalone research and was outside the scope of this article.

Methodology

All selected data were divided into two major groups: input and output. The input data consisted of the printout image, and internal and external printing-process parameters. Four internal parameters collected atline (viz. printhead movement velocity along the printing direction: "printing speed"; diameter, volume, and velocity of an ink droplet immediately after its ejection) characterized the system *printhead–nozzle orifice–ejected ink droplet*. Five external parameters collected online (viz. substrate temperature while printing; ambient air temperature and relative humidity, both while printing and sample measuring) described interfering environmental characteristics on the printing and on the measuring sites. The output data represented two print-independent manufacturing parameters (viz. distance between centers of adjacent deposited ink droplets: "drop space" {[ds]}; and post-treatment method {[M]}; both were stipulated by the experiment design), and two print-dependent PFS properties (viz. line resistance {[R]}; and presence of irregularities in the printout geometry: "line quality" {[Q]}). Thus, [ds] labelled the printing resolution, [R] the functional properties, [Q] the optical quality, and [M] the manufacturing process, all of which are essential quantifiers or qualifiers of a PFS. All output data had to be identified optically. To assess identification accuracy, corresponding output data were collected offline for each PFS. The process data along with their systematic, notation, units, and data type are summarized in Table 1. As indicated there, the output data consisted of both Boolean and non-Boolean types. Ergo, the task at hand required a sophisticated joint classification and regression analysis, specified in the following subsection *Performance Estimation*.

The workflow was divided into training and test phases. In the training phase, an evaluation model had to be generated based on the training dataset, which was formed from the interrelated input and output data (see Table 1). The evaluation model was the core of the algorithm that computed output data from the input data. During training, an iterative optimization of the model occurred: differential in the identified and the actual output data served for the fine-tune of the model features to minimize the error. For print-dependent [R] and [Q], an ancillary data benchmark was required to address variations in their actual values. In the test phase, an input data bench unknown to the optimized model had to be assessed. After processing of the bench, corresponding output data had to be returned without any further model improvement. Then, the ultimate accuracy of the derived output data had to be evaluated. [R] and [Q] had to be controlled additionally, considering their previously benchmarked actual values. The proposed workflow and all related data are schematically shown in Fig. 4. The PFSs indicated there are specified in the following subsection *Printed Functional Structures*.

Thus, the following stages had to be implemented within the scope of this work: (a) layout generation and manufacturing of printed structures; (b) collecting and processing of the input data; (c) elaboration and training of the CNN; (d) evaluation and accuracy assessment of the output data.

Inkjet-printing system and manufacturing process

A flatbed *Autodrop Gantry printing system* equipped with a 50 µm single-nozzle piezoelectric dispenser head *MD-K-140* (both manufactured by *microdrop Technologies*) was utilized for inkjet printing. One silver-nanoparticle (AgNP) based ink and one PET substrate, both commercially available and well-known, were applied for the sample fabrication. An extended description of the manufacturing processes, the post-treatment methods, and the applied materials is outlined in the SI.

Sample characterization and data collection

An in-house built automatic measurement system was employed offline for the optical and electrical PFS characterization. The system included a digital multimeter *DMM7510* (*Keithley)* for line resistance measurement, and a grayscale area-scan camera *acA2040-35gm* (*Basler)* with a 12 × optical system (*Navitar)* and a brightfield back/coaxial-forward illumination for an automatic image acquisition. Simultaneously, each obtained image was compared to the corresponding digital layout to evaluate optical quality of the PFS, as proposed by Gengenbach et al. (2020). Quality criteria are outlined in the following subsection *Printout Quality Assessment*. The ambient air temperature and humidity on the measurement site were logged online. Each sample was analyzed twice: before ([M] = {0}) and after ([M] = {1}) sintering in a hot-air oven (see SI for details). All collected data were stored in a machine-readable text format.

All non-image data had to be parsed and normalized to avoid random data errors. For the good-quality lines ([Q] = {1}), the maximum line resistance of 444 Ω was identified (sDS = 170 µm, non-sintered). In contrast, bad-quality lines ([Q] = {0}) demonstrated linear resistances over a wide range up to several MΩ that drastically increased data scattering. In turn, it unnecessarily increased values of the loss function, and decreased convergence during the CNN training. As a countermeasure, improper [R] values were deliberately equated to 10^3 Ω as the nearest higher power of 10. Erroneously collected non-positive [R] values were set to 10^3 Ω and esteemed as non-conductive.

Printed functional structures

A straight line of constant width (1D line) is the simplest design for determination of electrical resistance (Sowade

Table 1 Process data description

Process data					Data type
Group		Variable	Notation	Unit	
Input		Line printout	Grayscale image	Each px: [0, 1]	Normalized pixel array
	External	Substrate temperature (printing site)	t_s^o	[°C]	All: positive float
		Air temperature (printing site)	t_p^o	[°C]	
		Relative air humidity (printing site)	RH_p	[%]	
		Air temperature (measuring site)	t_m^o	[°C]	
		Relative air humidity (measuring site)	RH_m	[%]	
	Internal	Printing speed ($\propto$ jetting frequency)	υ_p	[mm/s]	Positive float
		Ink droplet diameter (prior to printing)	d_d	[µm]	Positive integer
		Ink droplet volume (prior to printing)	V_d	[pL]	Positive integer
		Ink droplet velocity (prior to printing)	υ_d	[mm/s]	Positive float
Output		Drop space (print-independent)	[ds]	[µm]	Positive integer
		Line resistance (print-dependent)	[R]	[Ω]	Positive float
		Line quality (print-dependent)	[Q]	{0, 1}	Boolean
		Post-treatment method (print-independent)	[M]	{0, 1}	Boolean

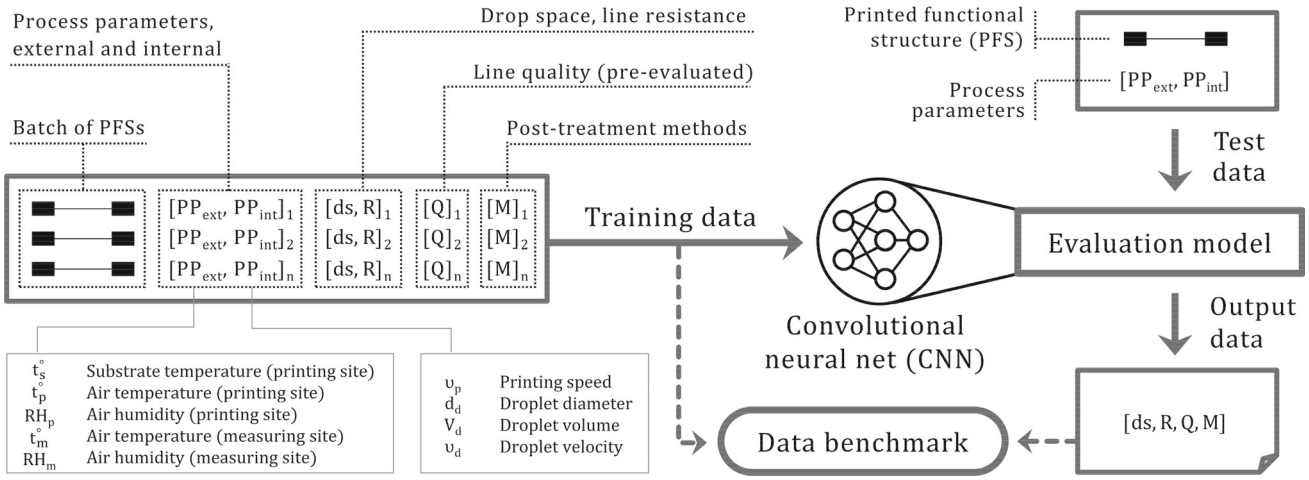

Fig. 4 Schematic representation of the proposed ML-based workflow. Set of training data encompassing PFS images and related process data have been utilized to generate an evaluation model. Then, output data have been identified from unknown PFS images using the model. Dashed lines represent ancillary stages for [R] and [Q]

et al., 2016; Ungerer, 2020). Due to its elementary shape, it is well-suited for detection of discrepancies between the digital layout and the printed outcome. The rapid and uncomplicated line manufacturing was beneficial for a prompt proof of the elaborated concept. In practice, printed 1D lines have been widely utilized as interconnects, interdigitated electrodes, and resistances (Sowade et al., 2016). An A5-sized layout generated as XML data is depicted in Fig. 5a. Each layout consisted of 60 individual PFSs ("bones") along with eight registration marks. Each bone was formed by a single-layered horizontal line with the digital width of 1 px, and by two contact pads on its ends (Ungerer, 2020). The drop space altered from line to line from 5 µm to 300 µm, with the 5 µm step size. In total, 60 different drop spaces were available in each layout. The digital layout is described in detail in the SI. In aggregate, 5,280 printed lines were fabricated and evaluated.

In contrast to the digital layout, the actual line width consistently varied depending on the drop space individually applied to each line ("set drop space" [sDS]). This effect can be observed in Fig. 5b, along with an area of satellite droplets occasionally emerged during printing. A photograph of a printed sample is depicted in Fig. S2 in the SI.

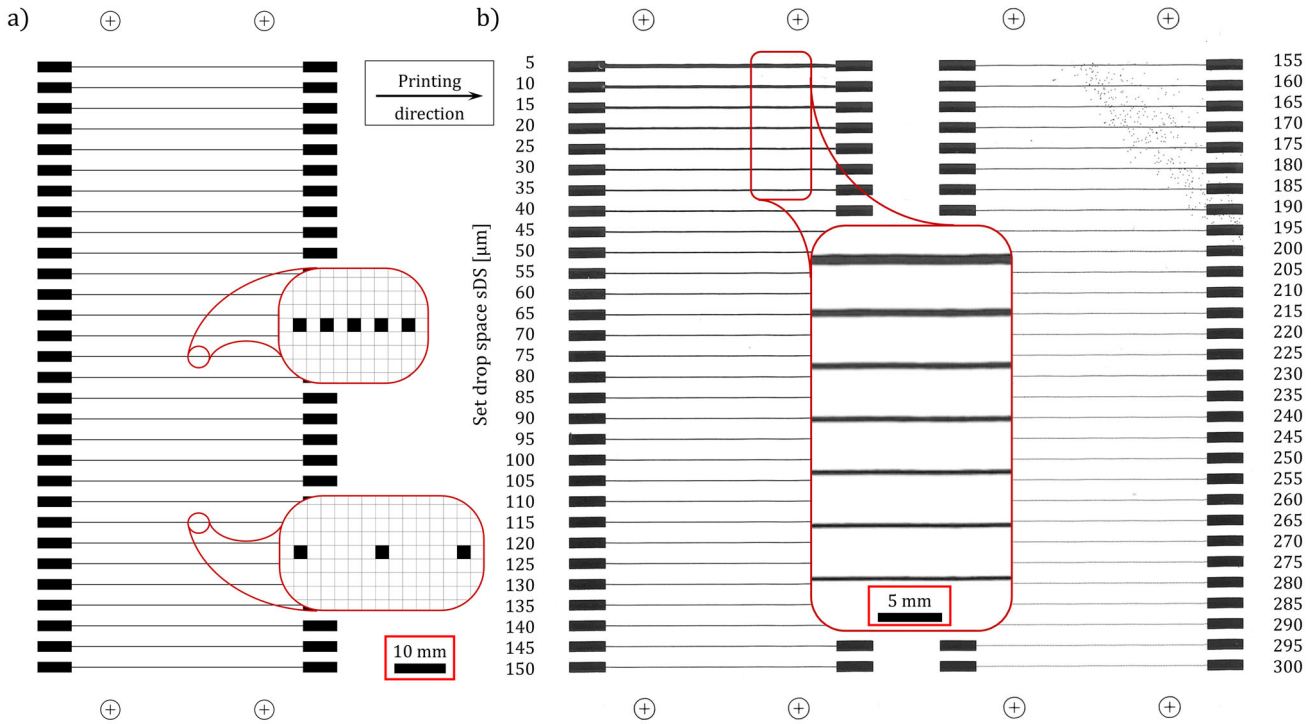

Fig. 5 **a** Part of the digital layout containing 30 individual lines and four registration marks above and below each column. The drop spaces vary from 5 µm (top line) to 150 µm (bottom line). Insets: schematic representation of the pixel allocation in a digital line (not true to scale and pixel number). **b** Complete inkjet-printed sample with 60 individual lines of various drop spaces and with eight registration marks. Inset: magnified lines with the drop spaces 5–35 µm. Lines with the drop spaces 5–20 µm are remarkably wider than the others due to the ink surplus. The line width decreases with the growing drop space value. An area polluted with occasional satellite droplets is visible in the top right corner

Printout quality assessment

Setup of the unidimensional sDS enabled us to fine-tune the optical quality and functionality (viz. line resistance) of the lines, since it changed the number of deposited ink droplets over the constant line length, as pointed out in Fig. 6a. Hence, it also changed a quantity of the deposited functional material and, therefore, line resistance. In this respect, the ratio of sDS to the diameter of a deposited ink droplet d_{dd} ("relative drop space" [rDS], rDS = sDS/d_{dd}, d_{dd} is represented in Fig. S1d in the SI) had the key impact on the printout quality. For rDS < 1, deposited ink droplets coalesce and form bound conductive lines. For rDS > 1, adjacent ink droplets are deposited too far apart and not able to coalesce in any proper way, the line remains completely or partly unbound. The corresponding change in the actual line width and shape while altering sDS and rDS is depicted in Fig. 6b–c.

Line geometry by rDS > 1 can be considered as *systematically irregular*. Along with that, sporadic printout defects can occur during the manufacturing process. Such defects usually arise through printhead and substrate impurities, local variations in the ink-substrate interaction, or incidental faults. Thus sporadic defects cause *non-systematic geometry irregularities*, the most common of which are demonstrated in Fig. 5d. In this work, only completely bound printed lines without any geometry irregularities were considered as good quality (i.e., with [Q] = {1}).

Machine learning

A supervised ML algorithm was elaborated: a plain neural net composed of four convolutional (CNN), and four fully-connected layers (multilayer perceptron). The *AdaM* optimizer (Schmidt et al., 2021; Sivaprasad et al., 2020) improved by the *Stochastic Gradient Descent with Warm Restarts* (SGDR) learning rate restart technique (Jha & Pant, 2021; Loshchilov & Hutter, 2017), the *SmoothL1* loss function (Wang et al., 2022), and the *Leaky ReLU* activation function (Abdel-Nabi et al., 2023; Dubey et al., 2022; Godfrey, 2019; Mercioni & Holban, 2020; Ogunsanya & Desai, 2022) were utilized. During an automatic image preprocessing, all auxiliary printout elements (i.e., contact pads and registration marks) were omitted. To mitigate computational overload, (a) a grayscale panoramic image of each line (see SI for details) was stepwise (b) cropped, (c) compressed

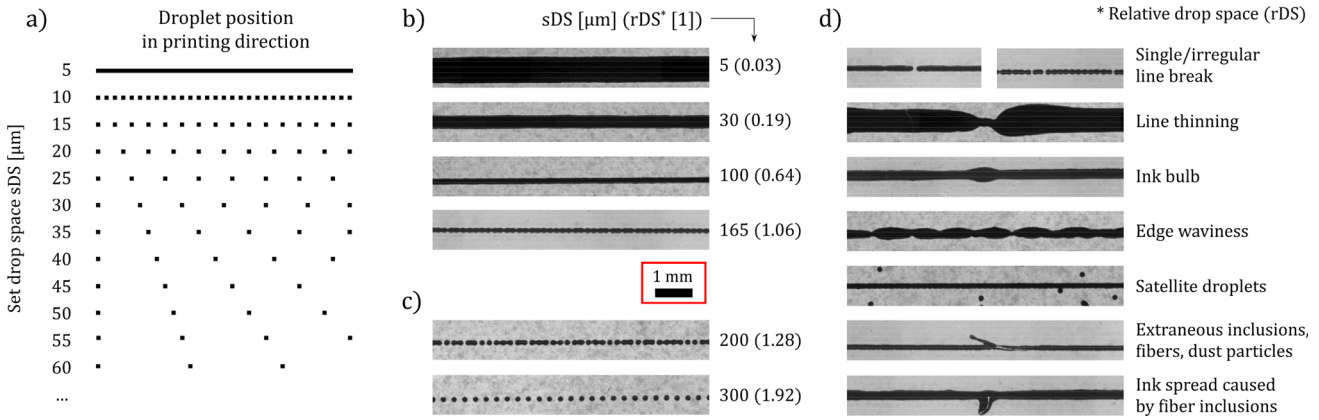

Fig. 6 **a** Simplified schematic representation of the deposited droplet position with regard to set drop space (not true to scale and droplet number), adapted from Sowade (2017, p. 45). **b–d** Enlarged view of individual printed lines: **b** bound lines printed with different drop spaces and without any visible irregularities in the line geometry; unbound lines with **c** systematic and **d** non-systematic irregularities in line geometry. Printed lines represented in **b** are considered as good quality ([Q] = {1}), and in **c–d** as bad quality ([Q] = {0}). The scale bar is integral for all images in **b–d**

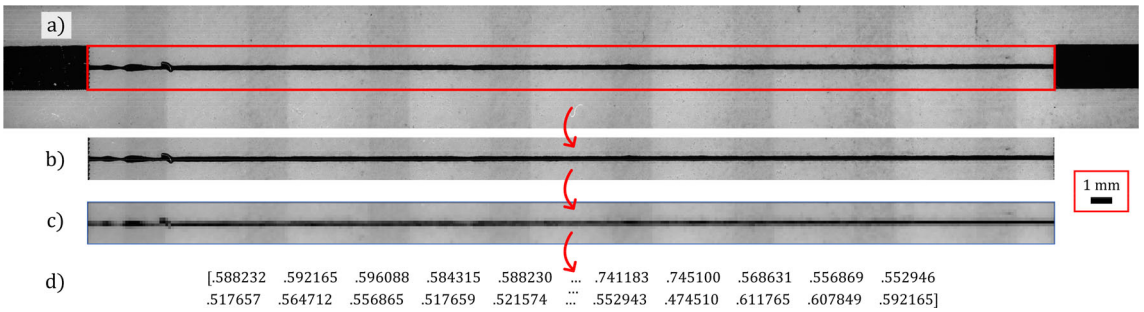

Fig. 7 Image data preparation. **a** Original panoramic printout image (14,202 × 1530 px), the red frame outlines the cropping area. **b** Cropped image prepared for the subsequent compression (12,190 × 490 px). **c** Compressed image ready as input data (2,400 × 60 px). **d** Normalized 2D pixel value array (2400 × 60 values; "0" correspond to 0% pixel brightness, "1" to 100%), exemplary values are indicated. All images are grayscale. The overlap zones (~ 26%) of individual frames of the panoramic image are clearly visible as wide darkened vertical stripes

to 2,400 × 60 px, and (d) transformed to a 2D array of normalized pixel values as demonstrated in Fig. 7. Expanded descriptions of the CNN and its architecture, of the pre-assessment of activation functions, and of the stepwise image pre-processing are provided in the SI.

Prior to model training, the complete input dataset was divided into a training, a validation, and a test set (60, 20, and 20 percent, respectively) using the *Random Split* method. 24 epochs were set for the CNN training, with an additional validation after each epoch to monitor the training process considering potential overtraining. The programming was carried out in *Python 3.11.5* and *PyTorch 2.0.1*.

Performance estimation

During training, validation, and test of the evaluation model, each output variable X according to Table 1 was attributed with two values: the actual one ("labeled value" [X^L]), and the one computed by the model ("predicted value" [X^P]). The output accuracy represented the concordance between X^L and X^P, and was anticipated to equal 1 for the complete match of X^L and X^P, and 0 for the complete mismatch (see accuracy diagram in Fig. S4 in the SI):

$$acc(X) = 1 - \frac{\left|X^L - X^P\right|}{\max\left(X^L,\, X^P\right)} \in [0,\, 1],\ 0 < X^L,\, X^P \leq 10^3. \tag{1}$$

The mean accuracy for all lines printed with a particular sDS was determined as

$$\overline{acc}_{sDS}(X) = \frac{1}{n_{sDS}} \cdot \sum_{i=1}^{n_{sDS}} acc(X_{i\,sDS}), \tag{2}$$

where n_{sDS} is the total number of the lines printed with a particular sDS, and X_{sDS} is the relevant output variable X solely for lines printed with a particular sDS.

For each output variable X, its mean actual value for all lines printed with a particular sDS was

$$\bar{X}^{L}_{sDS} = \frac{1}{n_{sDS}} \cdot \sum_{i=1}^{n_{sDS}} X^{L}_{i\,sDS}. \tag{3}$$

Since the accuracy function was supposed to evince varied elasticity for different sDS, the actual dispersion of the output values was assessed additionally. In particular, for [ds], the mean drop space error ($Err_{[ds]}$) was defined. It represented the effective error of the drop space identification, and was specified as a product of the mean [ds] accuracy for all lines printed with a particular sDS, and the latter itself:

$$Err_{[ds]} = \overline{acc}_{sDS}([ds]) \cdot sDS, \tag{4}$$

Analogously, the mean resistance error ($Err_{[R]}$) was specified for [R]. The effective error of the line resistance identification is a product of the mean [R] accuracy for all lines printed with a particular sDS, and the corresponding mean actual line resistance $\bar{[R]}^{L}_{sDS}$:

$$Err_{[R]} = \overline{acc}_{sDS}([R]) \cdot \bar{[R]}^{L}_{sDS}, \tag{5}$$

In the case of Boolean [Q] and [M], the accuracy function was expected to be non-elastic. For those variables, the effective error would be equal to their mean output accuracy. As a solution, classification via confusion matrix was performed (standard *classification accuracy* and *F-score* were applied as evaluation metrics).

An ancillary data benchmark of [R] and [Q] (see Fig. 4: *Data benchmark*) was conducted as a measure of the input data inequality, based on the assessment of expected standard deviations. A lower expected *SD* indicated a smaller variability in a dataset and, thus, a higher data repeatability. In turn, the latter was anticipated to positively correlate with the output accuracy. The mathematical expectation represents the weighted average of a dataset:

$$E(X) = \sum_{i=1}^{n} x_i \cdot p_i, \tag{6a}$$

where $x_1, x_2, \ldots$ are possible outcomes and $p_1, p_2, \ldots$ are corresponding probabilities for the variable X (Billingslay, 2012, pp. 81–84). In terms of the discontinuous sDS range set by the experiment design, the dataset consisted of finitely many discrete values. Since solely standard deviations of Boolean outcomes were of interest for us (i.e., [Q] = {0, 1}, {[R] = 10^3 Ω, [R] ≠ 10^3 Ω}), corresponding mathematical expectations for each sDS (vis. E_{sDS}[X]) were computed as

$$E_{sDS}(X) = \frac{n_{Bool}}{n_{sDS}} \cdot \sqrt{\frac{1}{n_{sDS}} \cdot \sum_{i=1}^{n_{sDS}} \left(X^{L}_{i\,sDS} - \bar{X}^{L}_{sDS}\right)^2}, \quad 0 \le n_{Bool} \le n_{sDS} \tag{6b}$$

where n_{Bool} is the amount of lines printed with a particular sDS and with the preset Boolean value.

Results

Input data benchmark

As stipulated by the experiment design, [ds] and [M] were equally distributed over all printed lines, with $p_{[ds]} = 1/60$ and $p_{[M]} = 0.50$, correspondingly. In contrast, print-dependent [Q] and [R] had a non-equal distribution over the sDS range. Benchmark results of two latter parameters are depicted in Fig. 8. Both variables demonstrated a strong negative correlation, and an equal value step transition at rDS≈0.9–1 (Fig. 8a). For bound lines, amount of the deposited functional material decreases with the sDS growth, as it was mentioned in the section *Printout Quality Assessment*. Accordingly, both $\bar{[Q]}^{L}_{sDS}$ and $\bar{[R]}^{L}_{sDS}$ tended to slightly accrue.

From the arrangement of mathematical expectation, pointed out in Fig. 8b, five quality groups were identified. (a) Firstly, for rDS ≤ 0.8 (sDS ≤ 125 μm), each deposited droplet firmly overlapped the adjacent one: a bound conductive line emerged (see Fig. 6b). Due to the minor number of bad-quality samples, caused mostly by occasional printout defects (e.g., by extraneous inclusions: see Fig. 6d), the E_{sDS}(X) remained small for such lines. (b) Within that area, PFSs with the rDS in the range 0.4–0.8 (sDS≈65–125 μm) featured the minimum spread of mathematical expectation values. The key reason of the decrease was the absence of a surplus of deposited ink, and, hence, the absence of thus induced geometry irregularities, such as ink bulbs and edge waviness. Therefore, such lines were expected to possess the best possible operational properties for printed electronics ("operational zone" [OZ]). (c) Respectively, the range rDS < 0.4 (sDS < 65 μm) could be conventionally denoted as a "pre-operational zone" (POZ). In the POZ, ink bulbs, edge waviness, and line thinnings (see Fig. 6d) were the typically occuring defects. (d) Secondly, for rDS ≥ 1.15 (sDS ≥ 180 μm), the deposited droplets had a substantial distance to the adjacent ones (see Fig. 6c). Since droplets stayed separate, formation of the bound condutive lines was not possible. Thus, the [Q] and [R] values remained constant, with *SD* and E_{sDS}(X) equal zero. (e) Lastly, for rDS

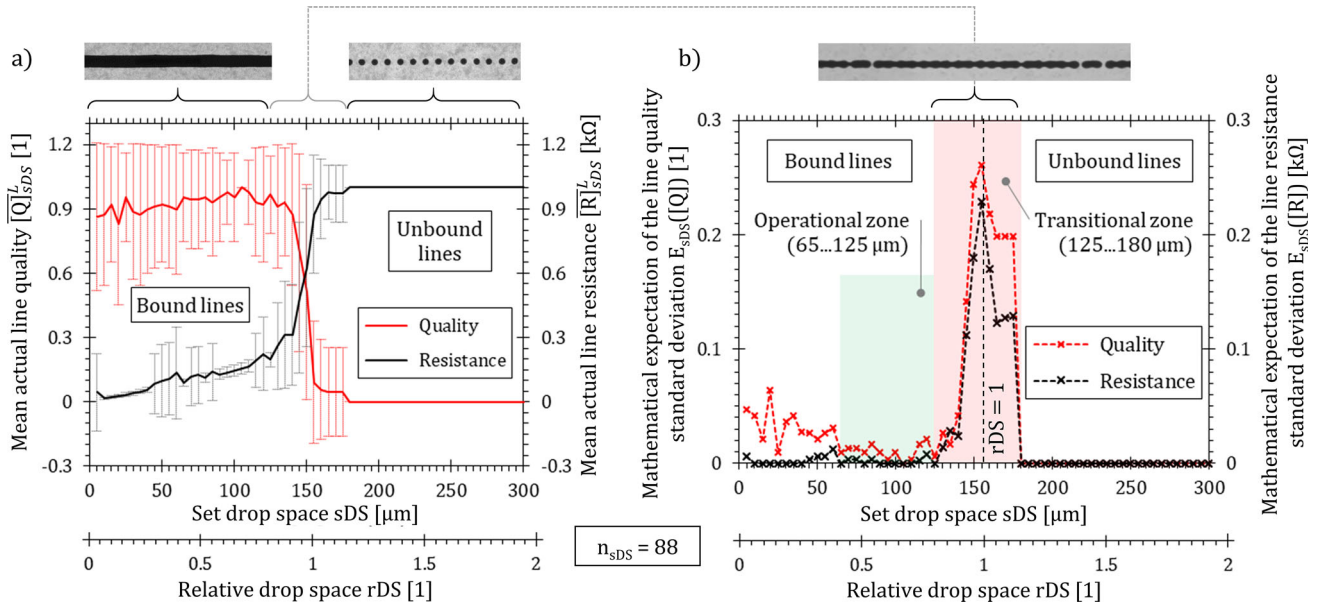

Fig. 8 **a** Variation of the mean actual [Q] and [R] values over the printed lines, with regard to sDS and rDS. For sDS ≥ 180 µm, $SD = 0$ for both variables. **b** Variation of mathematical expectation for the [Q] and [R] standard deviations, with regard to sDS and rDS. Lines printed with the drop spaces 30, 300, and 165 µm are shown as typical examples of bound, unbound, and transitional lines, respectively. In **b** Dashed lines link discrete values for greater clarity, without representing any continuous graph. Variability of $E_{sDS}([Q])$ at sDS < 65 is induced by the surplus deposited ink and related geometry irregularities in printed lines

Table 2 Description of the drop space quality groups

Quality group		sDS [µm]	rDS [1]	Characteristic printout features (see Fig. 6c–d)
1	Bound lines	0–125	0–0.8	Conductive bound lines with potential non-systematic geometry irregularities (incorporates both POZ and OZ)
1a	Pre-operational zone (POZ)	0–65	0–0.4	Conductive bound lines with a substantial line width and non-systematic geometry irregularities induced by the surplus of deposited ink
1b	Operational zone (OZ)	65–125	0.4–0.8	Conductive bound lines with the optimal line width and a small amount of both systematic and non-systematic geometry irregularities
2	Transitional zone (TZ)	125–180	0.8–1.15	Partly bound lines with a gradually increasing amount of systematic geometry irregularities
3	Unbound lines	≥ 180	≥ 1.15	Fully unbound, non-conductive lines composed of individual dots spaced apart

= 0.8–1.15 (sDS≈125–180 µm), formation of the firmly bound lines was unstable. Apparently, the major affecting factors were fluctuations in the ink droplet size, velocity, and placing accuracy; inhomogeneities in the substrate surface and in the ink-and-substrate interaction; and the ink-droplet coalescence behavior. The peak in Fig. 8b reveals a considerable amount of printouts demonstrating marginal [Q] and [R] values in the transition between bound and unbound PFSs ("transitional zone" [TZ]). The maximum $E_{sDS}(X)$ value in that zone corresponded to the sDS = 155 µm (rDS = 0.99) for both variables. We assumed, lines printed with rDS≈1—and more widely, within the entire TZ—would be the most challenging for the ML-based analysis. All identified quality groups are summarized in Table 2.

During the drying post-treatment ([M] = {0}), the solvent was evaporated from the deposited ink, and disperse AgNPs obtained an initial contact, partly agglomerating. The sintering post-treatment ([M] = {1}) was required to promote accretion of AgNPs, to remove organic additives, and to reduce structural discontinuities in the printed lines. Hence, electrical conductivity arose in sintered printed structures (Hussain et al., 2023; Perelaer et al., 2010). In our dataset, [R] values for the merely dried samples were considered as

100%. In turn, for the dried and subsequently sintered samples, [R] attained 85.7 ± 24.1% (all bound lines), and 76.5 ± 4.8% (all lines within the OZ).

Output data evaluation

Output accuracy for the variables [ds], [R], [Q], and [M] was evaluated with regard to sDS and rDS, and to the identified quality groups, to understand efficiency and boundaries of the elaborated ML algorithm. For [Q] and [M], the test data were classified by virtue of a confusion matrix. For [ds] and [R], the effective error values were computed from the relative output accuracy, based on the actual [ds] and [R] values. The evaluation results are aggregated in Fig. 9.

The mean output accuracy over the entire drop space range was not smooth, and differed among four output variables and five quality groups, as it can be noticed from Fig. 9a. Still, despite heterogeneity, certain trends could be clearly identified. The [ds], [R], and [Q] identification revealed a similar pattern of development with the sDS increase, with the best results for rDS > 1. The [M] identification was substantially less accurate, proceeded differently, and deteriorated with the sDS increase. In the POZ, all output variables accrued with a slight logarithmic trend (almost unnoticeable for [ds]), which was justified by a high elasticity of the accuracy function in that zone. In the OZ, all variables remained at large constant, despite some volatility. As it had been expected, a substantial descent was identified in the TZ for all output data. For rDS > 1, the [ds], [R], and [Q] values tended to reach a plateau with $\overline{\mathrm{acc}}_{\mathrm{sDS}}$([ds], [R], [Q])≈1.0. Similarly, with $\overline{\mathrm{acc}}_{\mathrm{sDS}}$([M])=0.56 ± 0.10, the mean identification accuracy of [M] remained virtually constant there, despite a vast accuracy variance, and could be considered as a genuine guessing. Regardless of the aforementioned direct dependency of [R] on [ds] (see Fig. 8a: *Bound lines*), the algorithm did not explicitly use one of those variables to determine the second one, as it can be seen in the inset of Fig. 9a.

Identification correctness of the Boolean [Q] and [M] is pointed out in Fig. 9b. For [Q], 1018 tested lines (96.40% of the test dataset) were classified correctly, with the F-score of 0.962. All six false-negative results were induced by impurities at the measuring site. The algorithm misclassified contaminations, such as dust and fibers under the transparent substrate (with the coaxial brightfield illumination) for local printed line defects, such as ink bulbs. That type of impurities is equally easy to mistake during a manual control (an example is represented in Fig. S3 in the SI). Furthermore, with the sDS range of 140–175 μm, those lines pertained to the TZ, which complicated the correct classification, as stated above. The 32 false-positive results did not consider existing non-systematic irregularities in the corresponding lines: preliminarily, single line breaks and ink bulbs (23 lines), and local edge waviness (7 lines). We supposed, that was implied by two key factors: (a) fuzzy transition between acceptable and extreme geometry irregularities, also inaccessible to the unambiguous identification by a person, and (b) information loss at image compression. For [M], 711 lines (67.33%) were identified correctly, with the F-score of 0.759. Any systematization of the false-negative results remained not attainable for [M], since no explicit rationale can have been identified. Among 285 false-positive results, 218 (76.50%) possessed rDS > 1, which were predominantly non-functional due to systematic geometry irregularities. The remaining part was evenly distributed between POZ, OZ, and TZ (approx. 8% each). We assumed that all false [M] identifications were impacted by loss of the sensitive image color information while image capturing and processing (a comparison of the sample appearance is presented in Table S2 in the SI). For unbound lines, due to the minimum printed area, the available color information was insufficient for the confident [M] detection, which seemed to be a reason of the guess-like result.

Yet, the reduced output accuracy at small sDS values, both $\mathrm{Err}_{[ds]}$ and $\mathrm{Err}_{[R]}$ were minor in the POZ (2.37 ± 1.36 μm and 8.48 ± 4.62 Ω, respectively), and slightly increasing in the OZ (2.96 ± 0.84 μm and 16.40 ± 6.14 Ω), as demonstrated in Fig. 9c. Both were rising rapidly within the TZ with the peak at sDS = 150 μm (rDS≈0.96) (7.07 μm and 140.91 Ω), with a subsequent decline to initial values for the unbound lines. The median error attained 2.00 μm for linewidth, and 5.65 Ω for resistance identification, collectively for all lines. Except for the TZ, the mean errors were satisfactory for practical use.

The point rDS = 1 undoubtedly separated the identification results into two accuracy groups (see Fig. 9a). For practically sensible conductive PFSs (rDS < 1), we gained the aggregate output accuracy of about 87.5%. Systematically unbound printed structures demonstrated output accuracies of over 99.3% for [ds], [R], and [Q]. However, the aggregate output accuracy remained around 88.7% in this area due to the insufficient [M] identification. The detailed accuracy apportionment over quality groups is highlighted in Fig. 9d–e.

CNN enlargement with further layers, both convolutional and linear, as well as increase in the channel number (see CNN design in Fig. S5 in the SI) did not reveal any visible result improvement. Vice versa, by reduction of the channel number eight times, and with two linear layers instead of four (illustrated in Fig. S8 in the SI), the aggregate output accuracy dropped by only a few percentage points. Output results of the contracted CNN are depicted in Fig. S9 in the SI. Similarly, a higher number of epochs while training induced overtraining, with corresponding accuracy deterioration (see output results for 24 training epochs in Fig. S10 in the SI).

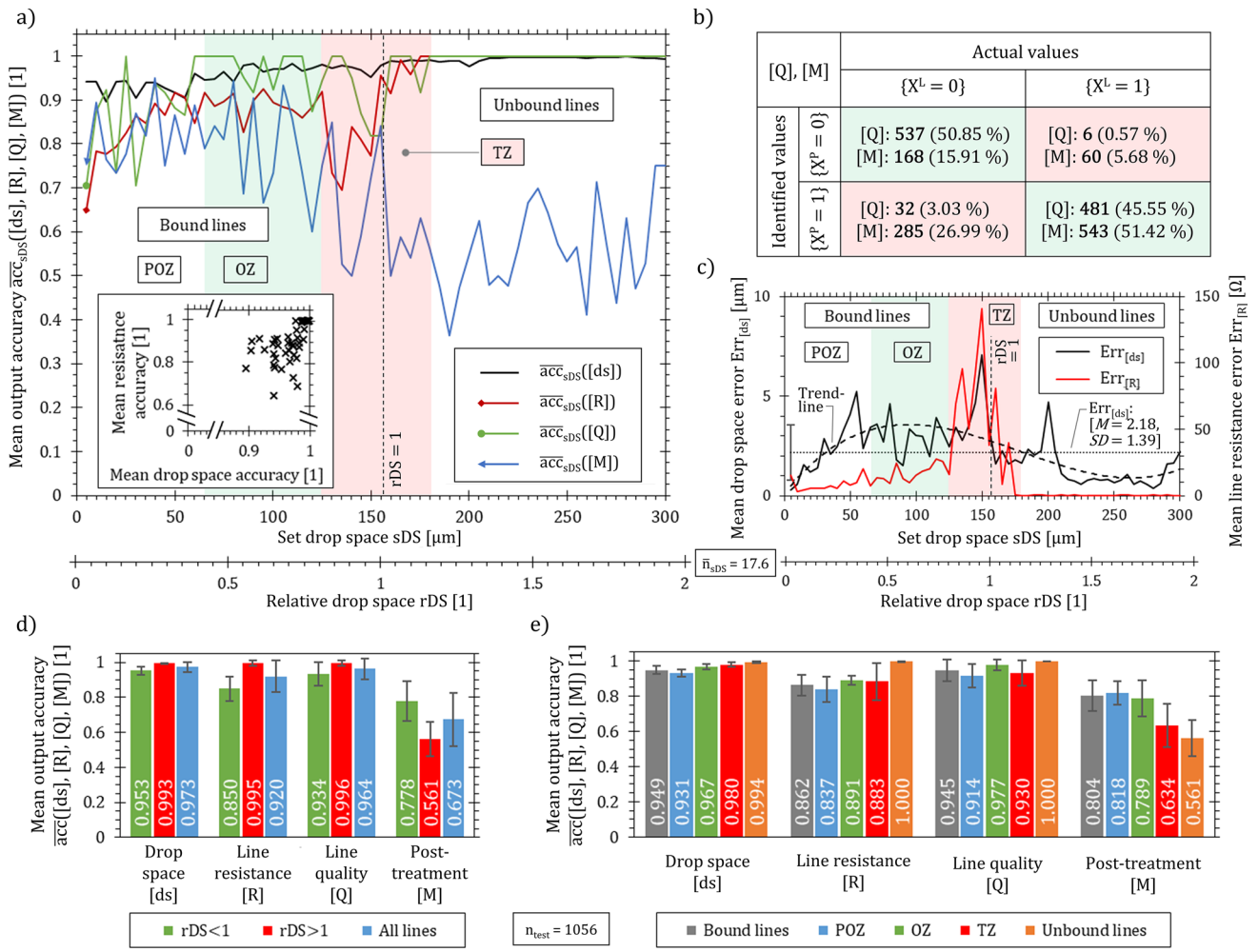

Fig. 9 **a** Mean output accuracy for the studied variables, with regard to sDS and rDS. Inset: mean [R] accuracy in relation to the mean [ds] accuracy, demonstrating the absence of any strong correlation between them. **b** Confusion matrix of the [Q] and [M] identification. Number of matching printed lines and corresponding percentage of the test dataset ($n_{test} = 1056$) are indicated for both output variables in each category. **c** Mean effective error of the [ds] and [R] identification, with regard to sDS and rDS. **d**–**e** Mean output accuracy for the studied variables, with regard **d** to rDS and **e** to quality groups

Discussion

Significance of selected output parameters

The output variables employed in this research (viz. drop space, line resistance, line quality, and post-treatment method) represent, correspondingly, printing resolution, functional properties, optical quality, and manufacturing method of a functional inkjet-printed product. They were selected as representing PFS properties of a different nature: appearance, functionality, quality, and fabrication, respectively. Reliable identification of the drop space (viz. sDS) enables an automatic inline control and adjustment of the printing resolution to obtain the optimal printout quality while printing. This leads to waste reduction and time saving during a fabrication process. Gengenbach et al. (2020) demonstrated a manual image-based identification of the actual drop space that lasted tens of minutes per sample. An added benefit is a quick subsequent identification of sDS for an arbitrary sample with lost fabrication data, or verification of such data. Optical identification of the line resistance is crucial for the damage-free evaluation of sensitive conductive layers. Identification of geometry irregularities is particularly important for the printed electronics with its decreased fabrication yield. Such quality identification allows to promptly sort out low-quality PFSs, and to tune the process parameters. Identification of the correct manufacturing method is significant for complex multi-step production processes. In the case of utilization of diverse post-treatment methods for diverse products, its correct identification is notably important at the collection point to sort out inappropriate samples. It is also crucial for an overview on the post-treatment quality. A ML-based inline monitoring of the drop space, of the type of emerging defects (i.e., systematic and non-systematic), and

the post-treatment method enables a dynamic control of their actual values, and an automatic tuning of the relevant process parameters to optimize the final product quality. An accurate simultaneous identification of all four selected parameters makes waste reduction, increase in the fabrication yield, and acceleration of the entire manufacturing process possible.

Impact of quality groups and printing resolution

For practically sensible bound lines (rDS < 1), identification accuracy is lower due to the more diverse PFS quality, to the presence of non-systemic geometry irregularities, and to the issues in the image quality. Still, identification of [ds] (95.3 ± 2.4%), and [Q] (93.4 ± 6.9%) approaching the 2-σ threshold can be considered as quite accurate. In the case of line resistance [R], the attained accuracy of 85.0 ± 7.0% seems to be sufficient for a practical application, due to the moderate effective error of 12.6 ± 6.8 Ω. The post-treatment method identification demonstrated an accuracy of 77.8 ± 11.4%. This value is anticipated to grow in the case of better-quality source images. In all cases, the best results are achieved in the quality group *Operational zone* possessing the minimal number of geometry defects (for [M]: in the *Pre-operational zone*, which proves, again, importance of the available graphic information about the PFS surface for this variable). For such samples, contamination through dust, fibers, dirt acts adversely on the identification, causing false-negative results.

For PFSs next to the tipping point rDS = 1, parameter identification remains less stable due to the highest variance of the sample quality. As a result, depending on the actual droplet diameter, a particular printed line can be bound or unbound. Both enhanced PFS image quality and size of the training dataset are absolutely vital to mitigate non-integrity of the training data, and, thus, to increase stability of the parameter identification. Stabilization of the fabrication process is substantial to avoid an increased instability of the sample quality at this point. However, the overall output accuracy in this complicated area can be considered as reliable enough (89.9% for sDS = 155 µm against 89.0 ± 5.6% for bound lines, for all output variables collectively).

For systematically bad-quality samples (rDS > 1), identification of the drop space, of resistance, and of the line quality tends to 100%, while identification of the post-treatment method declines sharply to around 56%. We assume, this is related to the available image quality: with clear and contrast printed-area edges for [ds] and [R], and with lacking information about color and texture of the printed area surface for [Q]. By contrast, Ivy et al. (2023) employed high-resolution color images of PFSs and derived sufficient information about the surface of inkjet-printed silver resistors. Hence, color, resolution, and an adequate contrast of PFS images are key for the PFS parameter identification. In addition, the dataset in this range is imbalanced due to the minimum quantity of good-quality samples. We believe, this is the major reason of the highest [Q] and [R] identification accuracy for unbound lines.

The attained results demonstrate a general efficiency of the proposed approach, and, thus, positively answer research questions Q1 and Q3. However, clear inequalities among identified quality groups validate significance of the relative drop space as a key parameter for the result interpretation. At large, bound lines possessing a natural quality variation show a slightly lower identification accuracy than unbound lines. PFSs within both *Pre-operational* and *Transitional zones* tend to have vastly more geometry defects caused by the amount of the applied material than within the *Operational zone.* Accordingly, parameter identification for the latter zone is comparatively more accurate, than for the former ones. In turn, printing resolution determines number of printed dots—hence, the material amount to be deposited on the substrate. In general, high printing resolution leads to deposition of the ink surplus, to ink spreading, and to emergence of sporadic PFS defects. Too low printing resolution is insufficient for an appropriate coalescence of ink droplets: a systematic edge waviness, or completely unbound lines occur. This is an answer to the research question Q4.

Limiting factors

We found out that quality of PFSs themselves, and quality of the PFS images are the principal limiting factors for the correct ML-based assessment of PFSs. For large and complex printed structures, to mitigate drastic increase in computing time, residual neural nets can be an appropriate solution, as shown by Kim et al., (2023a, 2023b). In contrast to sporadic small-size defects, systematic irregularities in printed structures do not require high-resolution images to be detected. Though, owing to the disappearance of small-size defects, reduction of the size and resolution of images captured for large-sized PFSs affects the identification robustness negatively and must be avoided.

Besides, we do not consider structures printed at an angle to the printing direction, typical for multi-nozzle raster-based inkjet-printing systems and for other large-area printing techniques (e.g., for screen printing). The effective printing resolution along angled edges is lower than the its set value. It affects the edge quality and, apparently, the line resistance, as Sowade et al. (2016) indicated. This does not apply to the single-nozzle system utilized for this work. However, impact of such structural features on the algorithm accuracy must be examined additionally in future work, owing to its utter importance for the field of printed electronics. We expect that owing to the edge quality deterioration, reported by Sowade et al. for angled PFSs, ML-based processing of such samples will tend to be less accurate. We assume, this negative effect

can be mitigated by incorporating of the angle value, and the relevant edge function proposed by Sowade et al. into the *internal process parameters* dataset (see Fig. 4).

Furthermore, the printed-layer thickness and cross-section profile are not addressed. Such structural information is apparently able to additionally improve identification of the fabrication method and of the functional properties, as reported by Hui et al. (2023) and Lall et al. (2023). If available, such structural information must be added to the *internal process parameters* dataset (see Fig. 4) to consider its impact on the parameter identification. However, collection of such information might require offline contact-based measurements, which apparently reduce feasibility and potential benefits of the proposed concept. In addition, surface color and texture were not fully incorporated into the datasets due to technical issues outlined in details in Table S2 in the SI. At availability, several interrelated images (e.g., acquired via ordinary scattered, inclined, or polarized light; 3D-scanned images, etc.) can be combined in an enhanced image dataset, providing supplementary information for a more accurate parameter detection.

CNN evaluation

We found out that a more sophisticated CNN does not essentially improve output accuracy. Apparently, the major reason is that a simple input image does not require sophisticated computations. Fast convergence (validation accuracy 0.883 after 4th epoch, 0.882 after 12th, 0.880 after 24th) indicates no need in the lasting CNN training (see Fig. S7 in the SI). An expanded dataset related to process parameters can be advantageous, however, we do not expect any significant improvement of the high accuracy attained. Other ML methods, such as *K-Nearest Neighbors*, *Random Forest*, *eXtreme Gradient Boosting*, *Residual Neural Networks*, or *Recurrent Neural Networks* can be in the best interest of the proposed algorithm, especially for solution of the classification problem, but require additional research. Similarly, a fine tuning of the CNN hyper-parameters can be beneficial. Still, identification of the best-performance ML method is outside the scope of this study.

The training time is 2.25 h per epoch (i.e., approx. 2.6 s per sample and epoch; PC specification is indicated in the SI). This time strongly depends not only on the CNN efficiency, but also on the image size, and cannot be directly compared with other studies. However, the training duration per epoch can be decreased by means of different ML architectures, as S. J. Kim et al., (2023a, 2023b) proposed. We noticed that image reduction leads to the significant acceleration of the training process, at cost of the reduced identification accuracy. Besides, 24 epochs are unambiguously redundant for training due to the fast convergence. For the pre-trained CNN, parameter identification on the test dataset of 1,056 randomly selected PFS images lasted around 23 s (i.e., approx. 22 ms per sample). By contrast, manual operations, such as contact-based resistance measurement and evaluation of the optical quality, require several to hundreds of seconds per sample. For non-experts, printing resolution and manufacturing method remain basically undetectable in manual operations. An automatic optical quality inspection reported by Gengenbach et al. (2020) and based on the *Bead Module* of the *Matrox Imaging Library* required tens of seconds for sample positioning, and up to hundreds of milliseconds per sample for the inspection, other parameters were not regarded in their study.

Further impacting factors

Along with the printing resolution, the following image and process-based factors have an impact on the algorithm accuracy:

- amount, quality, and integrity of the training data (i.e., a sufficient and balanced quantity of diverse, both good and bad quality samples),
- amount, quality, and integrity of available process-relevant parameters, both external and internal (i.e., material properties, environmental parameters, fabrication process parameters),
- presence and recognizability of visible geometry defects (e.g., edge waviness, satellite droplets, line breaks, etc.), systematization of such defects,
- presence of visual interference (e.g., dust particles, speckled background, etc.) in the image captured,
- availability of physical properties of the printed product (i.e., surface color, texture, and transparency; surface roughness and profile, cross-section area, roughness of edges printed at an angle, appearance of the coffee-ring effect, surface properties of the substrate, etc.),
- substrate planarity and form stability, illumination of the substrate while image capturing,
- image quality of the printed product (i.e., contrast, resolution, color space, image compression, etc.)

To a large extent, these factors affect availability and quality of visual information, essential for any image-based approach. In turn, they affect robustness of the proposed algorithm. The listed factors can be addressed by means of a thorough data preparation. Technical facilities, such as a high-resolution full-color camera with an advanced illumination system, inline and online sensors, robotics, are beneficial for an appropriate data collection. On the contrary, as previously mentioned, bigger images cause higher computational load and, hence, may be disadvantageous. In terms of the

speed performance, image data and its convolution constitute the major part of the data processing: in this study, 144,000-pixel data reshaped to a dataset of up to 27.7×10^6 values in the convolutional layers against nine process parameters and up to 256 channels in the multilayer perceptron. Utilization of more developed ML algorithms has to be considered to handle with this issue. Image augmentation increases amount of the training data and generalization of the model, and contributes to the higher output accuracy of the elaborated model. Although unchangeable internal process parameters and constant external factors do not affect quality of the CNN training, they slightly increase amount of the data and the computational load. Hence, such factors have to be omitted from the dataset as insignificant.

Yet, some factors are able to influence other ones indirectly. For instance, decrease in the substrate temperature can lead to a longer pinning time of the deposited ink droplet on the substrate. The same is true for the environmental impact on the ink rheology. In particular, in the case of the reduced surface tension, a bigger ejected droplet emerges and causes an increased diameter of a deposited ink droplet. In turn, more widely spread ink induces reduction of the relative drop space—up to transition to an adjacent quality group—despite the constant printing resolution. Stability and repeatability of the manufacturing process (e.g., ink droplet formation, ink and substrate interaction, etc.) have to be addressed to mitigate such data scattering.

Thus, this subsection provided an answer to the research question Q5.

Further fields of application

The developed algorithm enables an accurate simultaneous identification of various dissimilar properties of a printed functional product. It is beneficial for the future AI-assisted quality control in the PFS fabrication. The image-based approach can be easily tailored to an application with various printing techniques (e.g., screen, flexo, gravure printing, additive manufacturing, etc.), materials, and process parameters. It enables parameter identification from the printed product images acquired inline, atline, and offline, independent on the particular printing technique. Corresponding fabrication parameters (e.g., for screen printing: screen resolution and material, doctor-blade pressure and movement speed, printing paste viscosity, etc.) have to be considered in the *internal process parameters* dataset. We do not expect any critical application challenges as long as the aforementioned impacting factors are properly regarded.

Moreover, the proposed concept is suitable for a wide range of manufacturing processes beyond printing, such as in biomedical or chemical engineering. Its adjustable modular structure enables variability of the field of use depending on the required results. An image of the fabricated product remains the most crucial input data, along with its quality and integrity. The process and the output parameter datasets have to be tailored respectively. For instance, in the case of bioprinting of living cells, tissue viability has to be opted as a functional property; other output parameters remain intact. In the material, food, or chemical sectors, properties of compound crystals, granules, and powders (e.g., pellets, granulated food, fertilizers, etc.) can be assessed, as well. Thus, corresponding compound ratio has to be opted as a functional property, the grain size supersedes printing resolution, optical quality and manufacturing method remain intact. Still, a precise selection of the affecting parameters, and, first of all, recognizability of characteristic product features from its image is a considerable potential challenge for the ML algorithm. To handle with this problem, a scrupulous site-specific tuning of the image-capturing process and of the algorithm parameters might be needed.

In conjunction with the concept description provided in the *Introduction* section, this subsection is the answer to the research question Q2.

Conclusion

In this work, we conceptualize a ML-based approach to a multidirectional quality control in printed electronics. To validate the concept, we elaborate and study a CNN-based algorithm considering its ability to identify four parameters of a generic inkjet-printed functional structure collectively: drop space, line resistance, line quality, and post-treatment method. Broadly, these parameters correspondingly represent appearance, functionality, quality, and fabrication, all of which are substantial for a wide range of industrial products. We found that visual identification of dissimilar properties is feasible, but predictive power of the simple CNN-based algorithm is not equal for differently printed samples. Its efficiency noticeably depends (a) on setup parameters, such as printing resolution, (b) on stability and repeatability of the fabrication process, (c) on amount, quality, and integrity of the training data, (d) on type and systematization of geometry defects in the fabricated product, (e) on quality of the acquired images, and (f) on presence of visual interferences on the images. As we demonstrated, ratio of the distance between deposited droplets to their diameter (i.e., relative drop space) is an essential parameter for the result estimation, not yet considered by other research teams. Other impacting and limiting factors are discussed, potential avenues for transfer of the approach into further fields of application are proposed. In practical terms, the proposed concept enables advancement of quality control in high-throughput manufacturing processes, related to a wide range of industrial processes. Despite some revealed issues caused by the limiting factors, the proposed approach is able to reliably identify desired product properties.

In future work, optimization of the proposed approach, its transfer to a different domain within or outside of the printed-electronics area must be conducted. A performance comparison with other ML methods and fine-tune of hyperparameters must be addressed. The influence of the revealed affecting factors, both image and process-based, must be perceived and evaluated. Further combinations of data domains must be elaborated to prove flexibility of the proposed concept. Integration of the proposed algorithm as an inline quality control process will be a major step for the field of high-throughput manufacturing.

Supplementary Information The online version contains supplementary material available at https://doi.org/10.1007/s10845-024-02385-4.

Funding Open Access funding enabled and organized by Projekt DEAL. This work was funded by the program Material Systems Engineering of the Helmholtz Association (43.31.02). Open access funding enabled and organized by Project DEAL.

Declarations

Conflict of interest We have no known conflict of interest to disclose.

References

Abdel-Nabi, H., Al-Naymat, G., Ali, M. Z., & Awajan, A. (2023). HcLSH: A novel non-linear monotonic activation function for deep learning methods. *IEEE Access, 11*, 47794–47815. https://doi.org/10.1109/ACCESS.2023.3276298

Beedasy, V., & Smith, P. J. (2020). Printed electronics as prepared by inkjet printing. *Materials*. https://doi.org/10.3390/ma13030704

Billingslay, P. (2012). *Probability and measure* (Anniversary). Wiley.

Brishty, F. P., Urner, R., & Grau, G. (2022). Machine learning based data driven inkjet printed electronics: Jetting prediction for novel inks. *Flexible and Printed Electronics*. https://doi.org/10.1088/2058-8585/ac5a39

Carou-Senra, P., Ong, J. J., Castro, B. M., Seoane-Viaño, I., Rodríguez-Pombo, L., Cabalar, P., Alvarez-Lorenzo, C., Basit, A. W., Pérez, G., & Goyanes, A. (2023). Predicting pharmaceutical inkjet printing outcomes using machine learning. *International Journal of Pharmaceutics*. https://doi.org/10.1016/j.ijpx.2023.100181

Derby, B. (2010). Inkjet printing of functional and structural materials: Fluid property requirements, feature stability, and resolution. *Annual Review of Materials Research, 40*, 395–414. https://doi.org/10.1146/annurev-matsci-070909-104502

Dubey, S. R., Singh, S. K., & Chaudhuri, B. B. (2022). Activation functions in deep learning: A comprehensive survey and benchmark. *Neurocomputing, 503*(C), 92–108. https://doi.org/10.1016/j.neucom.2022.06.111

Flaig, M., & Zambal, S. (2021). Deep learning for zero-defect inkjet-printing of electronics. In *2021 IEEE international workshop on metrology for industry 4.0 & IoT (MetroInd4.0&IoT)* (pp. 458–463). https://doi.org/10.1109/MetroInd4.0IoT51437.2021.9488493

Gafurov, A. N., Phung, T. H., Ryu, B.-H., Kim, I., & Lee, T.-M. (2022). AI-aided printed line smearing analysis of the roll-to-roll screen printing process for printed electronics. *International Journal of Precision Engineering and Manufacturing-Green Technology, 10*, 339–352. https://doi.org/10.1007/s40684-022-00461-9

Gengenbach, U., Ungerer, M., Koker, L., Reichert, K.-M., Stiller, P., Allgeier, S., Köhler, B., Zhu, X., Huang, C., & Hagenmeyer, V. (2020). Automated fabrication of hybrid printed electronic circuits. *Mechatronics*. https://doi.org/10.1016/j.mechatronics.2020.102403

Godfrey, L. B. (2019). An evaluation of parametric activation functions for deep learning. In *2019 IEEE international conference on systems, man and cybernetics (SMC)* (pp. 141–145), IEEE. https://doi.org/10.1109/SMC.2019.8913972

Huang, J., Segura, L. J., Wang, T., Zhao, G., Sun, H., & Zhou, C. (2020). Unsupervised learning for the droplet evolution prediction and process dynamics understanding in inkjet printing. *Additive Manufacturing*. https://doi.org/10.1016/j.addma.2020.101197

Hui, J., Zhang, H., Lv, J., Lee, C.-H., Chen, C., Yan, Z., Wang, J., Peng, T., Guo, L., & Xu, Z. (2023). Investigation and prediction of nano-silver line quality upon various process parameters in inkjet printing process based on an experimental method. *3D Printing and Additive Manufacturing*. https://doi.org/10.1089/3dp.2022.0292

Hussain, A., Lee, H. L., & Moon, S. J. (2023). Sintering of silver nanoparticle structures and the pursuit of minimum resistivity. *Materials Today Communications*. https://doi.org/10.1016/j.mtcomm.2022.105159

Hutchings, I. M., & Martin, G. D. (Eds.). (2013). *Inkjet technology for digital fabrication*. Wiley.

Ivy, L., Xie, Y., Lobo, T., Gund, V., Davaji, B., Garud, M., Doerschuk, P., & Lal, A. (2023). Feature-based machine learning for predicting resistances in printed electronics. In *2023 IEEE international conference on flexible and printable sensors and systems (FLEPS)* (pp. 1–4), IEEE. https://doi.org/10.1109/FLEPS57599.2023.10220406

Jha, N., & Pant, D. R. (2021). Stochastic gradient descent and discriminative fine tuning on ResNet, DenseNet, Inception-ResNet and MobileNet for the multi class pathogenic microbes classification. In *10th IOE graduate conference (IOEGC)* (pp. 604–613), IOE. https://conference.ioe.edu.np/publications/ioegc10/ioegc-10-078-10108.pdf

Kim, E. J., Kim, J. H., Kim, M.-S., Jeong, S. H., & Choi, D. H. (2021). Process analytical technology tools for monitoring pharmaceutical unit operations: A control strategy for continuous process verification. *Pharmaceutics*. https://doi.org/10.3390%2Fpharmaceutics13060919

Kim, S., Cho, M., & Jung, S. (2022). The design of an inkjet drive waveform using machine learning. *Scientific Reports*. https://doi.org/10.1038/s41598-022-08784-y

Kim, S. J., Choi, E., Won, D. Y., Han, G., An, K., Kang, K.-T., & Kim, S. (2023b). Accelerated deep-learning-based process monitoring of microfluidic inkjet printing. *CIRP Journal of Manufacturing Science and Technology, 46*, 65–73. https://doi.org/10.1016/j.cirpj.2023.07.010

Kim, S., Wenger, R., Bürgy, O., Balestra, G., Jeong, U., & Jung, S. (2023a). Predicting inkjet jetting behavior for viscoelastic inks

using machine learning. *Flexible and Printed Electronics*. https://doi.org/10.1088/2058-8585/acee94

Kipphan, H. (Ed.). (2001). *Handbook of print media*. Springer.

Kwon, S. W., Kim, J. S., Lee, H. M., & Lee, J. S. (2023). Physics-added neural networks: An image-based deep learning for material printing system. *Additive Manufacturing*. https://doi.org/10.1016/j.addma.2023.103668

Lall, P., Soni, V., Kulkarni, S., & Miller, S. (2023). Comparison of machine learning approaches for correlating print process parameters to realized physical and electrical characteristics of printed electronics using inkjet platform. In *ASME 2023 international technical conference and exhibition on packaging and integration of electronic and photonic microsystems* (*InterPACK 2023*). https://doi.org/10.1115/IPACK2023-112056

Loshchilov, I., & Hutter, F. (2017). SGDR: Stochastic gradient descent with warm restarts. In *5th international conference on learning representations* (*ICLR*). https://doi.org/10.48550/arXiv.1608.03983

Maîtrejean, G., Samson, A., Roux, D. C. D., & El-Kissi, N. (2022). Rheological identification of jetted fluid using machine learning. *Physics of Fluids*. https://doi.org/10.1063/5.0100575

Mercioni, M. A., & Holban, S. (2020). The most used activation functions: Classic versus current. In *2020 international conference on development and application systems* (*DAS*) (pp. 141–145), IEEE. https://doi.org/10.1109/DAS49615.2020.9108942

Minnich, C., Hardy, S., & Krämer, S. (2016). Stopping the Babylonian confusion: An updated nomenclature for process analyzers in PAT applications. *Chemie Ingenieur Technik, 88*(6), 694–697. https://doi.org/10.1002/cite.201500188

Moon, S. K., Ng, N. P. H., Chen, L., & Ahn, D.-G. (2023). A novel quality inspection method for aerosol jet printed sensors through infrared imaging and machine learning. *CIRP Annals, 72*, 165–168. https://doi.org/10.1016/j.cirp.2023.03.029

Ogunsanya, M., & Desai, S. (2022). Predictive modeling of additive manufacturing process using deep learning algorithm. In *Proceedings of the IISE annual conference & expo 2022* (pp. 1–6). https://par.nsf.gov/servlets/purl/10335844

Ogunsanya, M., Isichei, J., Parupelli, S. K., Desai, S., & Cai, Y. (2021). In-situ droplet monitoring of inkjet 3D printing process using image analysis and machine learning models. *Procedia Manufacturing, 53*, 427–434. https://doi.org/10.1016/j.promfg.2021.06.045

Patterson, S. B. H., Wong, R., Barker, G., & Vilela, F. (2023). Advances in continuous polymer analysis in flow with application towards biopolymers. *Journal of Flow Chemistry, 13*, 103–119. https://doi.org/10.1007/s41981-023-00268-y

Perelaer, J., Smith, P. J., Mager, D., Soltman, D., Volkman, S. K., Subramanian, V., Korvink, J. G., & Schubert, U. S. (2010). Printed electronics: The challenges involved in printing devices, interconnects, and contacts based on inorganic materials. *Journal of Materials Chemistry, 20*, 8446–8453. https://doi.org/10.1039/C0JM00264J

Phung, T. H., Park, S. H., Kim, I., Lee, T.-M., & Kwon, K.-S. (2023). Machine learning approach to monitor inkjet jetting status based on the piezo self-sensing. *Scientific Reports*. https://doi.org/10.1038/s41598-023-45445-0

Schmidt, R. M., Schneider, F., & Hennig, P. (2021). Descending through a crowded valley—Benchmarking deep learning optimizers. In *Proceedings of the 38th international conference on machine learning* (*ICML*) (pp. 9367–9376), PMLR. https://proceedings.mlr.press/v139/schmidt21a.html

Shirsavar, M. A., Taghavimehr, M., Ouedraogo, L. J., Javaheripi, M., Hashemi, N. N., Koushanfar, F., & Montazami, R. (2022). Machine learning-assisted e-jet printing for manufacturing of organic flexible electronics. *Biosensensors and Bioelectronics*. https://doi.org/10.1016/j.bios.2022.114418

Siemenn, A. E., Shaulsky, E., Beveridge, M., Buonassisi, T., Hashmi, S. M., & Drori, I. (2022). A machine learning and computer vision approach to rapidly optimize multiscale droplet generation. *ACS Applied Materials & Interfaces, 14*(3), 4668–4679. https://doi.org/10.1021/acsami.1c19276

Singh, M., Haverinen, H. M., Yoshioka, Y., & Jabbour, G. E. (2013). Active electronics. In I. M. Hutchings & G. D. Martin (Eds.), *Inkjet technology for digital fabrication.* Wiley.

Sirringhaus, H., & Shimoda, T. (2003). Inkjet printing of functional materials. *MRS Bulletin, 28*, 802–806. https://doi.org/10.1557/mrs2003.228

Sivaprasad, P. T., Mai, F., Vogels, T., Jaggi, M., & Fleuret, F. (2020). Optimizer benchmarking needs to account for hyperparameter tuning. In *Proceedings of the 37th international conference on machine learning (ICML)* (pp. 9036–9045), PMLR. https://proceedings.mlr.press/v119/sivaprasad20a.html

Sowade, E. (2017). *Inkjet printing of photonic structures and thin-film transistors based on evaporation-driven material transportation and self-assembly* [Doctoral dissertation, Chemnitz University of Technology]. CORE. https://core.ac.uk/download/pdf/153230245.pdf

Sowade, E., Polomoshnov, M., & Baumann, R. R. (2016). The design challenge in printing devices and circuits: Influence of the orientation of print patterns in inkjet-printed electronics. *Organic Electronics, 37*, 428–438. https://doi.org/10.1016/j.orgel.2016.07.008

Stoyanov, S., & Bailey, C. (2017). Machine learning for additive manufacturing of electronics. In *40th international spring seminar on electronics technology (ISSE)* (pp. 1–6), IEEE. https://doi.org/10.1109/ISSE.2017.8000936

Teschner, H. (2010). *Druck- und Medientechnik: Informationen gestalten, produzieren, verarbeiten* [Print and media technology: Designing, producing, processing information] (13th ed.). Christiani

Tsai, M.-L., Qiu, R.-Q., Wu, K.-Y., Hsu, T.-H., Li, M.-H., & Lo, C.-Y. (2023). Machine-learning based characteristic estimation method in printed circuit board production lines. *Flexible and Printed Electronics*. https://doi.org/10.1088/2058-8585/ace4db

Ungerer, M. (2020). Neue Methodik zur Optimierung von Druckverfahren für die Herstellung funktionaler Mikrostrukturen und hybrider elektronischer Schaltungen [New methodology for the optimization of printing processes for the fabrication of functional microstructures and hybrid printed electronics]. *Automatisierungstechnik, 68*(9), 815–816. https://doi.org/10.1515/auto-2020-0103

Wang, Q., Ma, Y., Zhao, K., & Tian, Y. (2022). A comprehensive survey of loss functions in machine learning. *Annals of Data Science, 9*(2), 187–212. https://doi.org/10.1007/s40745-020-00253-5

Wenzel, V., & Nirschl, H. (2015). Validation of an inline particle probe in a high-shear mixer for particle size determination. *Powder Technology, 269*, 178–184. https://doi.org/10.1016/j.powtec.2014.09.003

Yan, K., Li, J., Pan, L., & Shi, Y. (2020). Inkjet printing for flexible and wearable electronics. *APL Materials*. https://doi.org/10.1063/5.0031669

Yan, Y., Yang, Q., Maize, K., Allebach, J. P., Shakouri, A., & Chiu, G. T. (2019). Image-based non-contact conductivity prediction for inkjet printed electrodes. In *Proceedings of the IS&T printing for fabrication: International conference on digital printing technologies (NIP35)* (pp. 152–157), IS&T. https://doi.org/10.2352/ISSN.2169-4451.2019.35.152

Zhao, M., Wei, H., Mao, Y., Zhang, C., Liu, T., & Liao, W. (2023). Predictions of additive manufacturing process parameters and molten pool dimensions with a physics-informed deep learning model. *Engineering, 23*, 181–195. https://doi.org/10.1016/j.eng.2022.09.015